

Thermomechanical Fatigue Behavior of a Directionally Solidified Ni-Base Superalloy

M. M. Shenoy

A. P. Gordon

D. L. McDowell

R. W. Neu¹

e-mail: rick.neu@me.gatech.edu

The George W. Woodruff School
of Mechanical Engineering,
Georgia Institute of Technology,
Atlanta, GA 30332-0405

A continuum crystal plasticity model is used to simulate the material behavior of a directionally solidified Ni-base superalloy, DS GTD-111, in the longitudinal and transverse orientations. Isothermal uniaxial fatigue tests with hold times and creep tests are conducted at temperatures ranging from room temperature (RT) to 1038°C to characterize the deformation response. The constitutive model is implemented as a User MATErial subroutine (UMAT) in ABAQUS (2003, Hibbitt, Karlsson, and Sorensen, Inc., Providence, RI, v6.3) and a parameter estimation scheme is developed to obtain the material constants. Both in-phase and out-of-phase thermo-mechanical fatigue tests are conducted. A physically based model is developed for correlating crack initiation life based on the experimental life data and predictions are made using the crack initiation model. [DOI: 10.1115/1.1924560]

Keywords: Constitutive Modeling, Crack Initiation, Directionally Solidified Superalloy, Fatigue Life Prediction

1 Introduction

Nickel-base superalloys are technologically significant materials that are used extensively in applications that require a material with high strength, good creep, and fatigue and corrosion resistance, even at elevated temperatures. Some of the applications include turbine blades, turbine discs, burner cans, and vanes. The operating temperatures of these components can range from room temperature (RT) to very high temperatures ($>1000^{\circ}\text{C}$) and they are exposed to complex mechanical loading superimposed with thermal transients; for example, creep deformation interacts with thermal and/or mechanical fatigue. Specialized processing techniques are employed to enhance mechanical properties, such as elimination of grain boundaries along the turbine blade axis by directional solidification. However, this introduces new challenges in constitutive modeling of the deformation behavior and life prediction.

The deformation mechanisms change with varying loads, orientations, strain rates, and temperatures. A physically based constitutive relation that can simulate the structural response in order to facilitate component life prediction should incorporate the active deformation mechanisms as a function of stress level, strain level, and temperature. The crystal plasticity approach provides a good compromise between manageability and modeling capabilities, especially when modeling components where the size, morphology, and crystallographic orientation of the grains control the anisotropic deformation behavior [1]. A physically based constitutive model is outlined to capture the homogenized deformation response in a directionally solidified superalloy, DS GTD-111. The material parameters are determined based on experimental low cycle fatigue (LCF) and creep data in both the longitudinal (L) and transverse (T) orientations. Fatigue tests with short hold times are also conducted to accurately capture the short-term primary creep behavior.

The combination of cyclic centrifugal forces experienced in blades at high temperatures in an aggressive environment, coupled with the heterogeneity and inherent anisotropy of the microstructure,

can lead to one of several possible damage mechanisms. Consequently, any physically based crack initiation model must capture the degradation mechanisms related to the microstructure and how they interact with the environment and cyclic inelastic behavior.

2 Material Microstructure and Composition

DS GTD-111 nickel-base superalloy has the chemical composition as shown in Table 1. The as-cast structure contains coherent, ordered γ' intermetallic precipitates dispersed uniformly in the austenitic γ phase as shown in Fig. 1. There is a bi-modal distribution of γ' precipitates, with cuboidal primary precipitates ($0.5\text{--}1\text{ }\mu\text{m}$) and spheroidal secondary precipitates ($0.05\text{--}0.2\text{ }\mu\text{m}$), with an overall volume fraction of approximately 46%. These precipitates are interspersed in the relatively soft matrix and are separated by the thin matrix channels. The grains are columnar and are roughly 125 μm long and 2 μm wide, which limits the role of grain boundaries in crack initiation. Primary dendrite stems grow parallel to the solidification direction. These stems are accompanied by secondary and tertiary dendrite arms, which grow outward along [100] and [010] directions. MC carbide inclusions, rich in Ti and Ta, are located in the interdendritic regions without any preferential orientation. The carbides are 50–150 μm long with a high aspect ratio ($\sim 10:1$ or greater). In addition to these carbides, M_{23}C_6 and γ/γ' eutectic nodules are located in the interdendritic channels. The γ/γ' eutectics are ductile and vary in size from 30 to 150 μm .

The observed deformation response in DS GTD-111 is consistent with that of other nickel base superalloys and can be summarized as follows [3]:

1. The yield strength increases with increasing temperature up to a peak temperature of 750°C , beyond which it decreases.
2. Slip is generally dictated by the resolved shear stresses along the favorable crystallographic slip planes. However, nickel base superalloys do not obey Schmid's law in all orientations and slip on any given plane can also depend on the resolved stresses on other planes (e.g., dislocation cross slip planes) due to dislocation core spreading effects in the γ' precipitates.

¹Author to whom correspondence should be addressed.

Contributed by the Materials Division for publication in the JOURNAL OF ENGINEERING MATERIALS AND TECHNOLOGY. Manuscript received October 5, 2004. Final manuscript received February 2, 2005. Review conducted by: R. Craig McClung.

Table 1 Nominal composition of DS GTD111

	Cr	Co	Al	Ti	W	Mo	Ta	C	Zr	B	Fe	Si	Mn	Cu	P	S	Ni
Min	13.7	9.0	2.8	4.7	3.5	1.4	2.5	.08	.005	.005	-	-	-	-	-	-	Bal.
Max	14.3	10.0	3.2	5.1	4.1	1.7	3.1	.12	.040	.020	.35	.30	.10	.10	.015	.005	Bal.

3. There is tension (T)-compression (C) asymmetry of the flow stress. The nature of this asymmetry is orientation and temperature dependent [4–8].
4. The initial yield behavior is nearly temperature path history independent, i.e., if a sample is first deformed at a high temperature at which the yield strength is high and then deformed at a low temperature, the material response is similar to a virgin material deformed at the lower temperature [9].

Any constitutive model should take these points into consideration.

3 Crystal Plasticity Formulation

A homogeneous constitutive model is proposed in this paper for which no explicit distinction is made between the matrix and precipitate phases. A crystal plasticity framework is employed to capture the orientation-dependent material response. As the temperature increases, strain rate effects are increasingly important and a rate-dependent method is employed. Crystal plasticity approaches have been used extensively in modeling single crystal superalloys [1,7,10] and the general methodology can be briefly described as follows. A multiplicative rule is used for the deformation gradient, \mathbf{F} , given as [11,12]

$$\mathbf{F} = \mathbf{F}^e \cdot \mathbf{F}^p \quad (1)$$

As shown in Fig. 2, the deformation gradient is separated into two parts: (i) the plastic deformation gradient (\mathbf{F}^p) formed due to dislocation motion, associated with a change in the shape of the grain but not its crystal lattice, and (ii) the elastic deformation gradient (\mathbf{F}^e), which essentially models reversible elastic stretch and rigid body rotation of the lattice. For any given lattice, the close-packed planes act as the slip planes with unit normal vector \mathbf{m}_o^α in the reference configuration for each of the α slip systems, along which the dislocations move in the slip direction in the reference configuration with unit vector \mathbf{s}_o^α . The shearing rates $\dot{\gamma}^\alpha$ along each of the active slip systems (α) depend on the resolved shear stress on the slip systems. The macroscopic plastic velocity gradient is obtained by summing over all slip systems in the intermediate relaxed configuration according to

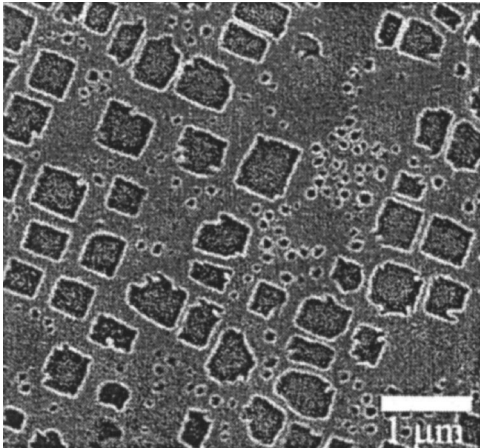


Fig. 1 Two-phase microstructure of DS GTD-111 superalloy [2]

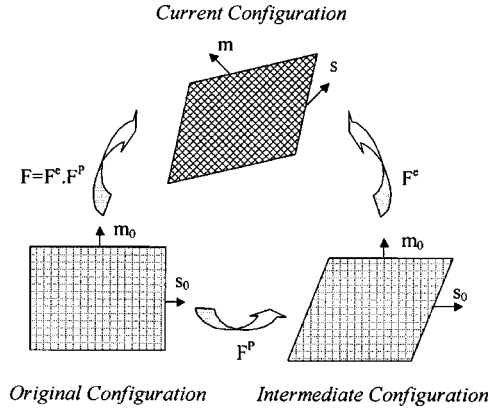


Fig. 2 Elastoplastic decomposition of the deformation gradient [11,12]

$$\mathbf{L}^p = \mathbf{D}^p + \mathbf{W}^p = \sum_{\alpha=1}^{N_{\text{slip}}} \dot{\gamma}^\alpha (\mathbf{s}_o^\alpha \otimes \mathbf{m}_o^\alpha) \quad (2)$$

where the plastic rate of deformation (\mathbf{D}^p) and plastic spin (\mathbf{W}^p) are given by the symmetric and anti-symmetric parts of the plastic velocity gradient, i.e.,

$$\mathbf{D}_{ij}^p = \frac{1}{2}(\mathbf{L}_{ij}^p + \mathbf{L}_{ji}^p), \quad \mathbf{W}_{ij}^p = \frac{1}{2}(\mathbf{L}_{ij}^p - \mathbf{L}_{ji}^p) \quad (3)$$

It should be noted that the intermediate, relaxed configuration in Fig. 2 is not unique since any superimposed rigid body rotation on the deformation gradient will also satisfy Eq. (1). Uniqueness of the intermediate configuration is obtained by assuming that the substructure spin is co-rotational with the lattice.

3.1 Constitutive Model. A rate-dependent crystal plasticity formulation is used. All slip systems are assumed active above the threshold stress, with the shearing rate of the α th system related to its associated viscous overstress by

$$\dot{\gamma}^\alpha = \dot{\gamma}_o \Theta(T) \left\langle \frac{\tau_v^\alpha}{D^\alpha} \right\rangle^n \exp \left\{ B_o \left\langle \frac{\tau_v^\alpha}{D^\alpha} \right\rangle^{n+1} \right\} \text{sgn}(\tau^\alpha - \chi^\alpha) \quad (4)$$

where the slip system viscous overstress τ_v^α is given in terms of the resolved shear stress τ^α by

$$\tau_v^\alpha = |\tau^\alpha - \chi^\alpha| - \kappa^\alpha \frac{\mu}{\mu_o} \quad (5)$$

Here, χ^α is the backstress and κ^α is the threshold stress on each slip system. Increase in the threshold stress leads to an increase in size of the viscoplastic flow potential, while the back stress results in a shift of the potential surface. The threshold stress may be viewed as the resistance to plastic flow arising from statistical strengthening mechanisms associated with an increase of dislocation density, solid solution strengthening, etc. The back stress displays a directional dependence and is associated with several features of the heterogeneous material at the microscale, including internal stresses that develop with deformation due to dislocation pile-up at obstacles such as precipitate particles, grain or phase boundaries, differential yielding with strain in hard (dislocation walls) and soft regions of the microstructure, and statistical interactions of dislocations bypassing barriers. Both back stress, χ^α , and the threshold stress, κ^α , depend on the history of temperature and viscoplastic deformation.

Equations (4) and (5) contain several other additional parameters defined as follows: $\dot{\gamma}_o$ is a reference shearing rate, n governs the power law creep regime, B_o and $(n+1)$ collectively govern the power law breakdown behavior at higher strain rates where the response becomes nearly rate independent, D^α is the drag stress that is weakly dependent on the history of temperature and visco-

plastic deformation when the behavior of the γ and γ' phases are homogenized, μ is the shear modulus, with μ_0 being the value of the shear modulus at absolute zero, and $\Theta(T)$ is the diffusivity parameter given by

$$\Theta(T) = \exp\left(-\frac{Q_o}{RT}\right) \quad \text{for } T \geq \frac{T_m}{2};$$

$$\Theta(T) = \exp\left\{-\frac{2Q_o}{RT_m} \left[\ln\left(\frac{T_m}{2T}\right) + 1\right]\right\} \quad \text{for } T \leq \frac{T_m}{2} \quad (6)$$

where Q_o is the activation energy for thermally activated dislocation bypass of obstacles, R is the universal gas constant, and T_m is the absolute melting point temperature.

The effective strain rate sensitivity exponent on the stress (inverse strain rate sensitivity) is given by

$$m = \frac{\partial \ln \dot{\gamma}^\alpha}{\partial \ln \tau^\alpha} = \frac{\partial \ln \dot{\gamma}^\alpha}{\partial \ln \tau_v^\alpha} = n + \frac{B_o(n+1)}{\hat{\tau}_o \mu / \mu_0} \left\langle \frac{\tau_v^\alpha}{\hat{\tau}_o \mu / \mu_0} \right\rangle^n \quad (7)$$

The anomalous yield behavior of γ - γ' nickel base superalloys, i.e., the yield stress increases with temperature in the intermediate temperature regime, is incorporated in the threshold stress. The anomalous behavior has been attributed to mechanisms involving $\{111\}$ $\langle 110 \rangle$ octahedral slip within the γ' precipitates. Several models attempt to explain this mechanism, including the Takeuchi and Karamoto model [13,14], the Paidar-Pope-Vitek (PPV) model [5], and the model proposed by Hirsch [15]. Though recent experimental evidence [16] seems to support the Hirsch theory, the PPV model has perhaps been the most widely used model [10], at least in the anomalous temperature regime (room temperature to 750°C).

According to the PPV model [5], in the anomalous behavior temperature regime (room temperature to 750°C) $\langle 10\bar{1} \rangle$ screw dislocations on (111) planes split into two super-Shockley partials separated by an antiphase boundary (APB). There are two configurations of the $a/2\langle 10\bar{1} \rangle$ screw dislocation: a glissile configuration with its core spread in the (111) plane and a sessile configuration with a nonplanar core spread in the $(1\bar{1}1)$ plane. The core transformation is explained in three steps: (i) constriction of the glissile core on the (111) plane, (ii) movement of the constricted dislocation along the (010) plane, and (iii) spreading of the dislocation on the $(1\bar{1}1)$ plane. The glissile core has to constrict first for this to happen; hence, any shear stress that aids in the constriction of the partial dislocations will assist cross-slip, leading to formation of sessile locks which act as obstacles to the glissile dislocations. Slip on the octahedral planes will be influenced by the stresses on the primary (step (i)) and secondary cross slip planes (step (iii)), along the direction perpendicular to the partial dislocations, as well as the stresses acting on the cube plane (step (ii)). The additional dependence of the activation enthalpy for the glissile to sessile transformation on the shear stress components (τ_{pe} , τ_{se} , and τ_{cb} , i.e., the shear stresses on the primary, secondary, and cube slip systems, respectively) leads to a non-Schmid effect. Since the enthalpy is also dependent on the sign of the stress components for steps (i) and (ii), it will differ in tension and compression. This leads to a tension-compression asymmetry that is orientation dependent. It should be noted that step (iii) is independent of the sense of loading.

To include the non-Schmid effects, the yield criterion for octahedral slip systems is modified based on the PPV theory as proposed by Qin and Bassani [17]. Each octahedral slip system is active only when the Schmid stress and a linear combination of the additional stress terms exceed a critical value, i.e.,

$$\tau^\alpha = h_{pe}\tau_{pe}^\alpha + h_{se}\tau_{se}^\alpha + h_{cb}|\tau_{cb}^\alpha| = \tau_{cr} \quad (8)$$

where τ_{pe} , τ_{se} , and τ_{cb} are the non-Schmid shear stresses and τ_{cr} is the critical resolved shear stress. This formulation is embedded in

the current set of constitutive relations through a critical threshold stress (κ^α), i.e.,

$$\kappa^\alpha = \kappa_c^\alpha + \kappa_e^\alpha \quad (9)$$

where

$$\kappa_c^\alpha = \kappa_o^\alpha(T) + h_{pe}\tau_{pe}^\alpha + h_{se}\tau_{se}^\alpha + h_{cb}|\tau_{cb}^\alpha|$$

and

$$\kappa_e^\alpha = h_o \sum_{\beta=1}^{N_{slip}} q^{\alpha\beta} |\dot{\gamma}^\beta| - h_{ks} \kappa^\alpha \sum_{\beta=1}^{N_{slip}} |\dot{\gamma}^\beta| - h_s \Theta(T) (\kappa^\alpha - \kappa_{th})^{r_s}$$

The back stress evolution for homogenized γ - γ' models can be written in the hardening-dynamic recovery plus static thermal recovery format as

$$\dot{\chi}^\alpha = h_\chi |\dot{\gamma}^\alpha| \text{sgn}(\tau^\alpha - \chi^\alpha) - h_{\chi d} \chi^\alpha |\dot{\gamma}^\alpha| + \left(\frac{1}{R_\chi} \frac{\partial R_\chi}{\partial T} + \frac{1}{h_{\chi d}} \frac{\partial h_{\chi d}}{\partial T} \right) \chi^\alpha \dot{T} - \Omega_\chi^\alpha \quad (10)$$

where $\Omega_\chi^\alpha = h_{\chi s}(T) |\chi^\alpha|^{r_{\chi s}}$ is the static thermal recovery term, h_χ , $h_{\chi d}$, $h_{\chi s}$, $r_{\chi s}$ are material parameters, and $R_\chi = h_\chi / h_{\chi d}$. The temperature-rate-dependent term is necessary to properly model hysteresis behavior under thermomechanical fatigue (TMF) [18], since the model parameters that govern the back stress evolution rates are themselves functions of temperature. Note that for single phase models, the back stress evolution equation can likely be neglected, but it is essential to describe the overall average behavior of the crystallographic grains in homogenized γ - γ' models. It is a very significant fraction of the flow stress (typically > 30%) for Ni-base superalloys [19]. The constitutive equations are summarized in Table 2.

4 Experiments

Test sections were sectioned from two batches of cast plates. Solid specimens with a uniform gage length of 12.7 mm (0.5 in.) and a diameter of 6.35 mm (0.25 in.) were machined from sections oriented in the longitudinal (L) and transverse (T) directions. The specimen was prepared according to ASTM Standard E606 [20]. Tests were performed on a 45 kN (10 kip) axial servo-hydraulic MTS testing machine with dual-channel controllers and TestStar software (Testware SX 4.0D). Load, strain, and temperature data were recorded digitally. The tests were conducted under mechanical strain control using an extensometer with ceramic tips in direct contact with the specimen to obtain the total strain. The mechanical strain ratio $R_\epsilon = \epsilon_{\min} / \epsilon_{\max}$ was held constant at $R_\epsilon = -1$. An Ameritern 2 kW RF induction heater provided heat to the specimens. Five K-type thermocouples were directly attached to the specimen (three within the gage section) to achieve a near-uniform temperature distribution within the gage section, and the induction coil was iteratively modified to achieve a maximum gage section temperature variation of either 1% of T_{\max} or ± 3 K. For both LCF and TMF tests, the temperature was maintained using a PID temperature controller. In TMF tests, the temperature reading was transmitted to the TestStar controller and used to calculate the components of thermal and mechanical strain. By following the procedural guidelines in ASTM E2368 [21], TMF testing can accurately simulate damage caused by the combined effects of thermal cycling and mechanical fatigue. Prior to each test, a relationship for thermal strain ($\epsilon_{th}(T)$) is determined using the free response under unloaded thermal cycles. This correlation is replayed during TMF cycling. Thus, all TMF tests were conducted using closed-loop, temperature-based thermal strain control. A total of 36 strain-controlled isothermal LCF tests and 5 TMF tests were conducted, as shown in Table 3. Three types of cycles were used: continuous cycling with (a) no hold time (CC),

Table 2 Summary of constitutive model

Flow Rule:

$$\dot{\gamma}^{\alpha} = \dot{\gamma}_0 \Theta(T) \left\langle \frac{\tau_v^{\alpha}}{D^{\alpha}} \right\rangle^n \exp \left\{ B_0 \left\langle \frac{\tau_v^{\alpha}}{D^{\alpha}} \right\rangle^{n+1} \right\} \text{sgn}(\tau^{\alpha} - \chi^{\alpha})$$

where

$$\tau_v^{\alpha} = |\tau^{\alpha} - \chi^{\alpha}| - \kappa^{\alpha} \frac{\mu}{\mu_0} \quad \text{and} \quad D^{\alpha} = D_0 \frac{\mu}{\mu_0}$$

$$\Theta(T) = \exp \left(-\frac{Q_0}{RT} \right) \quad T \geq \frac{T_m}{2}$$

$$\Theta(T) = \exp \left\{ -\frac{2Q_0}{RT_m} \left[\ln \left(\frac{T_m}{2T} \right) + 1 \right] \right\} \quad T \leq \frac{T_m}{2}$$

Evolution Equations for Hardening Variables:

Back stress

$$\dot{\chi}^{\alpha} = h_{\chi} |\dot{\gamma}^{\alpha}| \text{sgn}(\tau^{\alpha} - \chi^{\alpha}) - h_{\chi d} \chi^{\alpha} |\dot{\gamma}^{\alpha}| + \left(\frac{1}{R_{\chi}} \frac{\partial R_{\chi}}{\partial T} + \frac{1}{h_{\chi d}} \frac{\partial h_{\chi d}}{\partial T} \right) \chi^{\alpha} \dot{T} - \Omega_{\chi}^{\alpha}, \quad R_{\chi} = h_{\chi} / h_{\chi d}$$

$$\text{where } \Omega_{\chi}^{\alpha} = h_{\chi s} \Theta_{\chi s}(T) |\chi^{\alpha}|^{r_{\chi s}}, \quad \Theta_{\chi s}(T) = \Theta(T)$$

Threshold Stress

$$\kappa^{\alpha} = \kappa_c^{\alpha} + \kappa_e^{\alpha}, \quad \kappa_c^{\alpha} = \kappa_0^{\alpha}(T) + h_{pe} \tau_{pe}^{\alpha} + h_{se} \tau_{se}^{\alpha} + h_{cb} |\tau_{cb}^{\alpha}|$$

$$\dot{\kappa}_e^{\alpha} = h_0 \sum_{\beta=1}^{N_{slip}} q^{\alpha\beta} |\dot{\gamma}^{\beta}| - h_{\kappa s} \kappa^{\alpha} \sum_{\beta=1}^{N_{slip}} |\dot{\gamma}^{\beta}| - h_s \Theta(T) \langle \kappa^{\alpha} - \kappa_{th} \rangle^{r_s}$$

$$\text{Initial conditions: } \chi^{\alpha}(0) = 0, \quad \kappa_e^{\alpha}(0) = 0$$

(b) with 2 min hold time in tension (HT), and (c) with 2 min hold time in compression (HC). A constant strain rate of 0.005 s^{-1} was used during the loading and unloading ramps.

The cycles to crack initiation in Table 3 is defined as the number of cycles at which a 20% drop in the maximum axial load occurred. In many instances, the cycle with the critical load drop-off coincided with complete fracture of the gage section.

5 Implementation and Determination of Material Parameters

The constitutive model was implemented as User MATERIAL (UMAT) subroutine in ABAQUS [22], based on the implicit integration scheme of McGinty [23]. A hyperelastic formulation was used, valid for arbitrary finite strain. A time step subincrementation scheme and a linear search algorithm were employed in the constitutive subroutine to ensure convergence.

It is assumed that the flow rule given in Eq. (4) is suitable for modeling the homogenized γ - γ' phases, but with a much higher intrinsic lattice friction necessary to model the higher activation energy for slip compared to modeling only a single phase, such as γ . It is commonly observed that the creep exponent of Ni-base superalloys is more or less invariant with respect to γ' volume fraction and morphology, suggesting that slip is indeed restricted in the precipitates, which provide primary elevated temperature strength.

The 12 octahedral $\{111\}\langle 110 \rangle$ slip systems are appropriate for FCC single crystals and are active for the entire temperature range. The six cube slip systems $\{100\}\langle 110 \rangle$ type (three planes and two directions=six systems) may be active at high homologous temperatures and high resolved shear stress (in γ' phase), but their role is less well understood and characterized. A precise mechanism is still largely conjectural, since the identification of the role

Table 3 Test matrix for isothermal LCF and TMF. (a) Test matrix for TMF in longitudinal (L) and transverse (T) orientations using in-phase (IP) and out-of-phase (OP) thermomechanical loading histories. Cycle type CC—continuous cycling without hold time, Cycle type 2 min C—continuous cycling with 120 s hold time at peak strain in compression, Cycle type 2 min T—continuous cycling with 120 s hold time at peak strain in tension. (b) Test matrix for isothermal LCF in longitudinal orientation and (c) test matrix for isothermal LCF in transverse orientation.

Specimen Number	Grain Orientation	Phasing	Temperature (°C)	Mechanical Strain Range, $\Delta\epsilon_m$ (%)	Plastic Strain Range, $\Delta\epsilon_{pl}$ (%)	Thermal Strain Range, $\Delta\epsilon_{th}$ (%)	Cycles to Failure, N_f
L8-11A	L	OP	538 \rightleftharpoons 927	1.0	0.19	0.53	149
L-8-10A	L	OP	539 \rightleftharpoons 927	0.5	0.02	0.61	1371
L8-9	L	IP	538 \rightleftharpoons 1038	1.0	0.19	0.89	66
T8-10	T	OP	538 \rightleftharpoons 927	1.0	0.44	0.53	17
T8-10A	T	OP	538 \rightleftharpoons 927	0.5	0.10	0.53	173

(a)

Specimen Number	Temperature (°C)	Cycle Type	Total Strain Range, $\Delta\epsilon_t$ (%)	Elastic Strain Range, $\Delta\epsilon_{el}$ (%)	Plastic Strain Range, $\Delta\epsilon_{pl}$ (%)	Stress Range, $\Delta\sigma$ (MPa)	Cycles to Initiation, N_i
L8-4	427	CC	2.00	1.33	0.67	1805	10
L8-6	649	2 min C	1.00	0.97	0.03	1220	6761
L8-3A	760	CC	2.00	1.67	0.33	1826	83
L8-2A	871	CC	4.00	1.17	2.83	1240	11
GTD-CC10	871	CC	2.00	1.18	0.82	1068	223
GTD-CC05	871	CC	1.00	0.94	0.06	896	1410
GTD-CC04	871	CC	0.80	0.76	0.04	758	3700
L8-3	871	CC	0.50	0.50	0.01	537	29159
GTD-HT10	871	2 min T	2.00	1.32	0.68	1240	21
GTD-HT05	871	2 min T	1.00	0.86	0.14	896	691
GTD-HT04	871	2 min T	0.80	0.75	0.05	847	213
GTD-HC10	871	2 min C	2.00	1.36	0.64	1344	48
GTD-HC05	871	2 min C	1.00	0.89	0.11	827	450
GTD-HC04	871	2 min C	0.80	0.78	0.02	758	301
L8-8	982	CC	2.00	0.82	1.18	696	100
L8-4A	982	CC	1.00	0.66	0.34	636	569
L8-8A	982	CC	1.00	0.65	0.35	653	509
L8-9A	982	CC	0.80	0.56	0.24	551	960
L8-5	982	2 min T	1.00	0.67	0.33	599	285
L8-5A	982	2 min C	1.00	0.89	0.11	827	114
L8-6A	982	2 min C	0.50	0.46	0.04	413	271
L8-7A	1038	CC	1.00	0.56	0.44	449	570
L8-7	1038	2 min C	1.00	0.53	0.47	413	535

(b)

Specimen Number	Temperature (°C)	Cycle Type	Total Strain Range, $\Delta\epsilon_t$ (%)	Elastic Strain Range, $\Delta\epsilon_{el}$ (%)	Plastic Strain Range, $\Delta\epsilon_{pl}$ (%)	Stress Range, $\Delta\sigma$ (MPa)	Cycles to Initiation, N_i
T8-1	871	CC	4.00	1.17	2.83	1647	3
T8-1A	871	CC	2.00	1.11	0.89	1702	10
T8-2	871	CC	1.00	0.93	0.07	1378	293
T8-5	871	CC	0.80	0.58	0.22	847	610
T8-2A	871	CC	0.51	0.51	0.00	813	16069
T8-5A	871	2 min HT	1.00	0.67	0.33	1089	181
T8-6A	871	2 min HC	1.00	0.67	0.33	1144	86
T8-3A	982	CC	1.00	0.57	0.43	703	207
T8-4	982	CC	1.00	0.55	0.45	758	212
T8-4A	982	2 min HT	1.00	0.75	0.25	799	44
T8-3	982	2 min HC	1.00	0.52	0.48	717	401
T8-7	1038	CC	1.00	0.55	0.45	572	112
T8-7A	1038	2 min HC	1.00	0.72	0.28	558	152

(c)

of cube slip is challenging. For homogenized γ - γ' single crystals, the role of cube slip is usually assessed by considering the breakdown of the capability of octahedral slip to model the stress-strain-time behavior as a function of temperature, which of course depends on other elements of the constitutive framework. The work of Bettge and Osterle [24] on SC16 has revealed that mac-

roscopic cube slip is a manifestation of octahedral slip and takes place by multiple cross slip events on octahedral planes, producing zig-zag dislocation lines. This enables the dislocations to travel large distances along matrix channels, thus effectively shearing material along the cube planes. In addition, actual cube slip has been observed [16] in the γ' precipitates at higher tem-

peratures and along orientations closer to [111]. Experimentally, softening occurs as the orientation is rotated from the [100] orientation [25]. When only octahedral slip is active, hardening is predicted as the loading axis is rotated from the [100] direction, which is inconsistent with experimental observation. Both sources of cube slip, zig-zag cross slip in the γ phase and motion of dislocation segments on cube planes in the γ' phase, are lumped together in the present model, treated via the activation of the cube slip systems. Both the octahedral and cube slip systems are assumed to be active in this model at all times.

The material parameters for the octahedral slip systems are determined from data obtained from uniaxial cyclic loading of longitudinal specimens along the [100] orientation, for which the loading axis is oriented along the grain growth direction. Cube slip is not activated in this orientation for small deformations. The material parameters for the cube slip systems are obtained using data from transverse specimens (loading perpendicular to the grain growth direction) due to lack of data in other orientations. It should be noted that the response of directionally solidified material in the transverse orientation is an average response comprising several grains. A total of 30 grains with random transverse orientations are used to obtain this average behavior along the loading axis. The Taylor constraint for intergranular interactions is assumed in this averaging process, such that each grain (with different orientations along the transverse direction) is subjected to the same deformation gradient; this approach is convenient in that a single element can be used to obtain the initial estimate of the material parameters, and is sufficiently accurate for slip of polycrystals with high symmetry cubic structures. A more rigorous finite element analysis is subsequently run with 30 hexagonal grains, each containing 96 elements, to optimize the fit of material parameters.

Under cyclic loading, lattice rotation may be insignificant, but in the presence of creep or cyclic ratcheting, lattice rotation may build up at sites of stress concentration or near interfaces such as grain boundaries. However, the creep and ratcheting strains are small in the cyclic loading experiments conducted to determine the material parameters, so these lattice rotations are neglected for the purpose of estimating the material parameters. Several other simplifications can be made regarding the deformation behavior of this material at this temperature. In the temperature range under consideration, the precipitate structures (size, shape, morphology) are stable, so higher-scale microstructural changes such as coarsening of precipitates can be neglected in the evolution equations.

From the cyclic deformation data, it is observed that the initial yield strength does not change significantly with cyclic loading. This indicates that the threshold and drag stress are nearly constant and that the backstress is the primary internal state variable that evolves with deformation. The threshold stress is mainly limited to the critical value κ_c^α that incorporates non-Schmid terms as previously explained, and the drag stress (D^α) is kept constant. The remaining material parameters must be physically admissible. This calls for a systematic procedure for determining the constants. First, certain physical parameters such as elastic properties and activation energies of thermally activated diffusional processes are obtained from literature. The activation energy is set to $Q=309$ kJ/mol, based on the data from Daleo and Wilson on GTD-111 [26]. Estimating the remaining material parameters by using graphical methods in the analysis of deformation data is often not possible with viscoplasticity models because there is a strong coupling between creep and cyclic plasticity. Approximate values of the material parameters can often be obtained, but a trial-and-error approach almost always must be employed to refine the parameters to accurately capture the experimental deformation response. A more robust and efficient approach is to integrate the constitutive model, simulating the actual loading histories, using an optimization scheme to iteratively evaluate the model parameters [27].

The general optimization scheme involves running several

simulations involving different thermomechanical histories including cyclic deformation with and without hold periods, as well as creep deformation, using a set of parameters suggested by the optimization code. Then the model response is compared to the actual experimental response generating a value of an objective function defined on the basis of the norm of the error between the experimental and predicted deformation responses. The Epogy code by Synaps [28] is used to minimize the objective function by iteratively modifying the material parameters based on minimization of the objective function. Epogy employs four widely used search methods (linear simplex, downhill simplex, gradient, and genetic algorithms) to assure stability and enhance the probability that an optimum set of material parameters will be obtained among various local minima. The rate of convergence and effectiveness of the optimization is highly dependent on the objective function, which in turn depends on the type of loading history. For uniaxial cyclic loading, the error function is defined as

$$\text{Error} = \sum_i (\sigma_{\text{exp}}^i - \sigma_{\text{pre}}^i)^2 W_i \quad (11)$$

where σ_{exp}^i is the experimentally measured stress along the loading direction, σ_{pre}^i is the stress predicted by the model at the same strain, and W_i is a weighting parameter for the i th strain value. The weighting parameter is varied from 0.8 to 1.2, depending on which region of the stress-strain response is being simulated. Less weight is placed on the elastic portions of the deformation ($W_i=0.8$) while $W_i=1.2$ is used during inelastic flow. During strain hold periods in which inelastic deformation and stress relaxation occurs, $W_i=1.0$.

Since the static thermal recovery terms are influential only for long hold periods and into the steady state creep regime, these terms can be neglected in the preliminary parameter estimation exercise that uses only continuous cycling data without hold times. The results of this preliminary exercise provides tighter bounds on those parameters that are less sensitive to rate for purposes of later optimization exercises that include cyclic data with strain holds and creep data intended to refine the estimates of material parameters. The error norm used for estimating parameters associated with creep behavior is

$$\text{Error}_{\text{creep}} = \sum_i (\epsilon_{\text{exp}}^i - \epsilon_{\text{pre}}^i)^2 E_{\text{av}}^2 \quad (12)$$

where $\epsilon_{\text{exp}}^i - \epsilon_{\text{pre}}^i$ is the difference between experimentally measured strain and predicted strain at a given time instant. This error norm employs the average value of the Young's modulus, E_{av} , in the specified orientation to scale the errors in terms of pseudo-stresses. For this final optimization step, the total error is the sum of the errors for the cyclic and creep deformation data,

$$\text{Error} = \text{Error}_{\text{cyclic}} + \text{Error}_{\text{creep}} \quad (13)$$

The material parameters obtained are listed in Table 4. Some of the material parameters are not listed due to unavailability of experimental data for fitting parameters. Static thermal recovery effects in evolution of κ are omitted, for example. Accordingly, dashed entries in Table 4 signify zero values of the parameters.

The most sensitive material parameters for this data set as determined by the optimization scheme are $h_{\chi d}$ and $h_{\chi s}$, which control the backstress evolution. It should be noted that backstress plays an important role in Ni-base superalloys. Based on the tests by Ferney et al. [29] and Latif et al. [30], it could be to the order of 50%–60% of the flow stress. Experimental data used to fit parameters and correlated simulations based on the constitutive model are compared in Figs. 3–9.

6 Thermomechanical Fatigue (TMF)

For TMF, a deformation gradient \mathbf{F}^θ based on the thermal expansion is included in the multiplicative decomposition of the

Table 4 Material parameters: (a) octahedral slip system constants $\chi^\alpha(0)=0$, $\kappa_e^\alpha(0)=0$; (b) cube slip system constants $\chi^\alpha(0)=0$, $\kappa_e^\alpha(0)=0$; and (c) common constants

Temperature (°C)	h_x (MPa)	R_x (MPa)	h_{xs}	r_{xs}	κ_o^α (MPa)	h_o (MPa)	h_{ks}	h_s	r_s	$q^{\alpha\beta}$
427.0	55160	110.0	-	-	93.0	6895	135	-	-	1
760.0	186165	148.0	2.37E-7	1	148.0	0	0	-	-	-
871.1	137900	92.0	7.77E-8	1	70.0	0	0	-	-	-
982.2	41370	69.0	-	-	14.0	0	0	-	-	-
1037.8	17238	64.3	-	-	14.0	0	0	-	-	-

(a)

Temperature (°C)	h_x (MPa)	R_x (MPa)	h_{xs}	r_{xs}	κ_o^α (MPa)	h_o (MPa)	h_{ks}	h_s	r_s	$q^{\alpha\beta}$
427.0	-	-	-	-	-	-	-	-	-	-
760.0	-	-	-	-	-	-	-	-	-	-
871.1	172400	81.2	-	1	64.2	0	0	-	-	-
982.2	55160	54.5	-	-	11.0	0	0	-	-	-
1037.8	17238	44.8	-	-	11.0	0	0	-	-	-

(b)

Temperature (°C)	C_{11} (MPa)	C_{12} (MPa)	C_{44} (MPa)	n	B_o	μ (MPa)	h_{pe}	h_{cb}	h_{se}
427.0	169617	70675	132000	5	0.05	132000	0.15	0.1	-0.03
760.0	151690	70329	125750	5	0.05	125750	0.15	0.1	-0.03
871.1	138830	69980	120360	4	0.05	120360	0.0	0.0	0.0
982.2	134450	69980	113880	4	0.05	113880	0.0	0.0	0.0
1037.8	131000	69980	108180	4	0.05	108180	0.0	0.0	0.0

(c)

Q_o (KJ/mol)	R (J/mol K)	μ_o (MPa)	$\dot{\gamma}_o$ (s ⁻¹)	κ_{th} (MPa)	D_o (MPa)
309	8.314	166000	1.15×10^9	0.0	102.0

(c)

deformation gradient. An intermediate, thermally expanded, hot unstressed configuration and a hot plastically deformed relaxed configuration are introduced [31]. Thus the total deformation gradient is given by $\mathbf{F}=\mathbf{F}^e \cdot \mathbf{F}^p \cdot \mathbf{F}^\theta$, where the linearized elastic deformation is described by \mathbf{F}^e , the plastic deformation by \mathbf{F}^p , and the thermal expansion/contraction by \mathbf{F}^θ . Assuming isotropic thermal expansion, the velocity gradient associated with thermal expansion effects is given as

$$\mathbf{L}_o^\theta = \dot{\mathbf{F}}^\theta \cdot (\mathbf{F}^\theta)^{-1} = \alpha \dot{\theta} \mathbf{I} \quad (14)$$

where α is the thermal expansion coefficient (assumed constant) and \mathbf{I} is the second rank identity tensor. Solving the differential equation over a time step gives

$$\mathbf{F}_{t+\Delta t}^\theta = \exp(\mathbf{L}_o^\theta \Delta t) \mathbf{F}_t^\theta \quad (15)$$

Material parameters are assigned temperature dependence using third-order interpolative polynomial fits of values determined for isothermal cyclic loading cases. The temperature is updated and

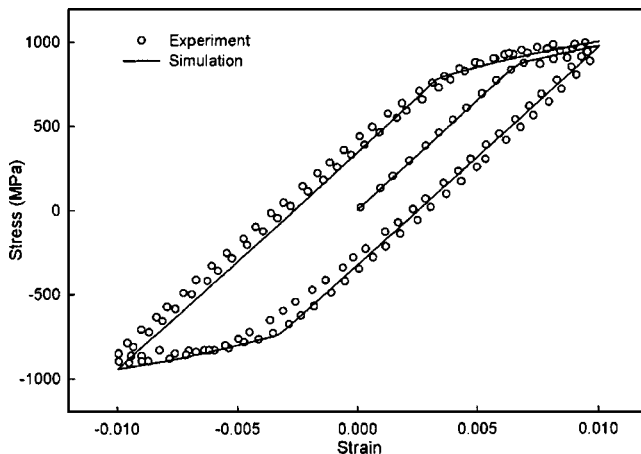


Fig. 3 Stress-strain response: experimental data and correlated simulations at 427°C (longitudinal, CC, first cycle)

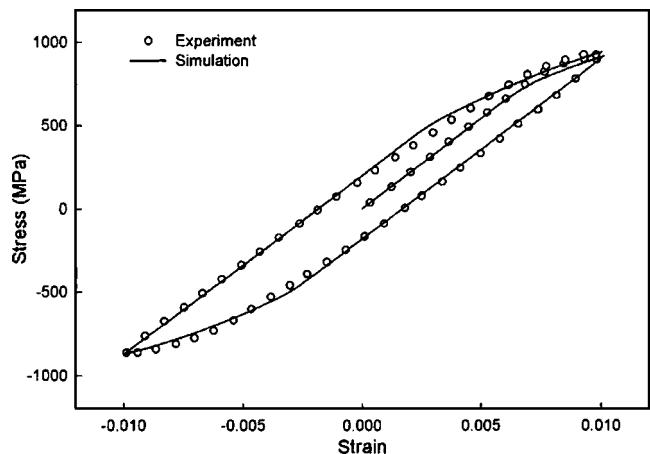


Fig. 4 Stress-strain response: experimental data and correlated simulations at 760°C (longitudinal, CC, first cycle)

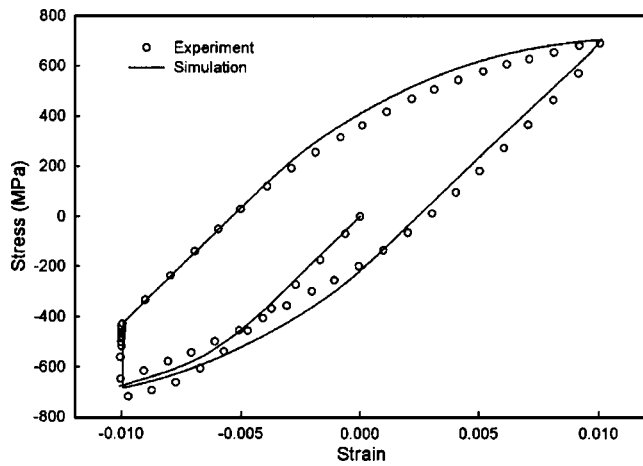


Fig. 5 Stress-strain response: experimental data and correlated simulations at 871°C (longitudinal, HC, first cycle)

held constant for each Newton Raphson step and the material parameters relevant to that temperature are used. These TMF simulations can be considered as true predictions which correlate reasonably well with the experimental results for loading in both the longitudinal and transverse orientations, as shown in Figs. 10–12.

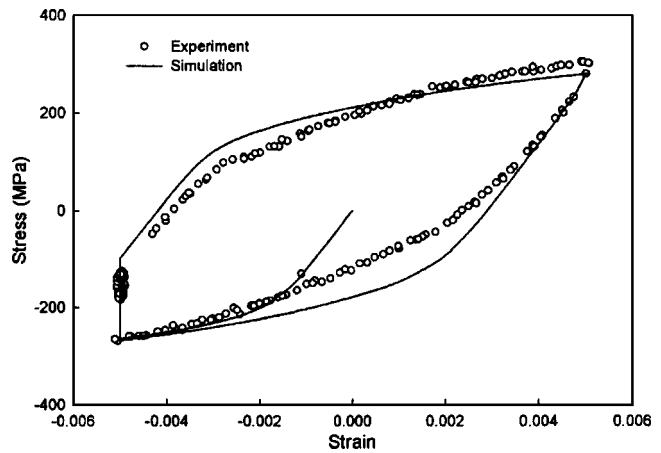


Fig. 8 Stress-strain response: experimental data and correlated simulations at 1038°C (transverse, CC, first cycle)

7 Fatigue Crack Initiation

The crack initiation life is defined as the number of cycles at which the load drops below 20% of the initial maximum stabilized tensile load. The constitutive model described above is used to predict the cyclic material response under imposed isothermal and

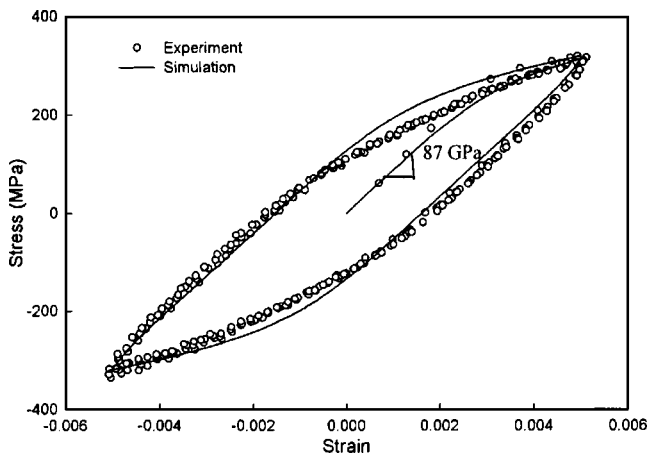


Fig. 6 Stress-strain response: experimental data and correlated simulations at 982°C (longitudinal, CC, first cycle)

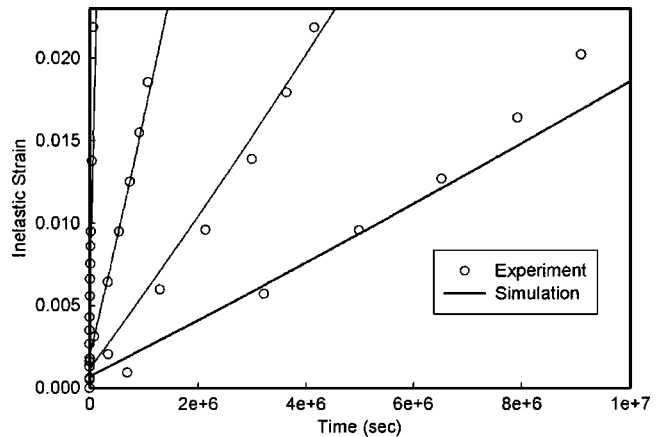


Fig. 9 Primary and secondary creep responses: experimental data and correlated simulations at 871°C (longitudinal)

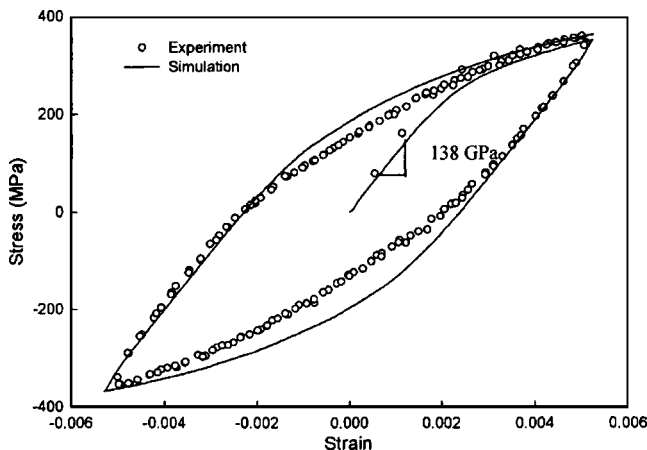


Fig. 7 Stress-strain response: experimental data and correlated simulations at 982°C (transverse, CC, first cycle)

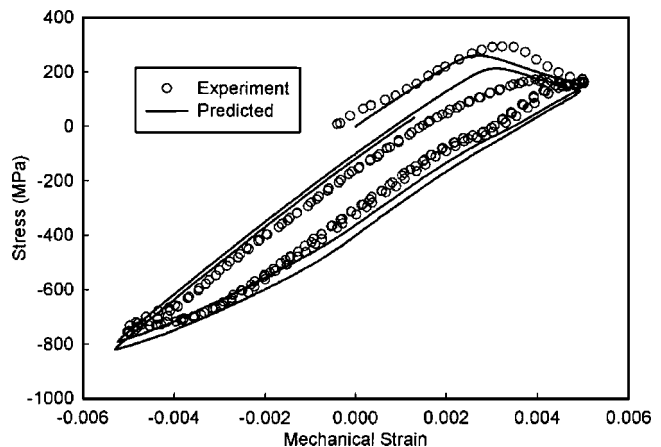


Fig. 10 Stress-strain response: comparison of experimental data with model predictions for in-phase (IP) TMF 538°C–1038°C in the longitudinal orientation (first cycle)

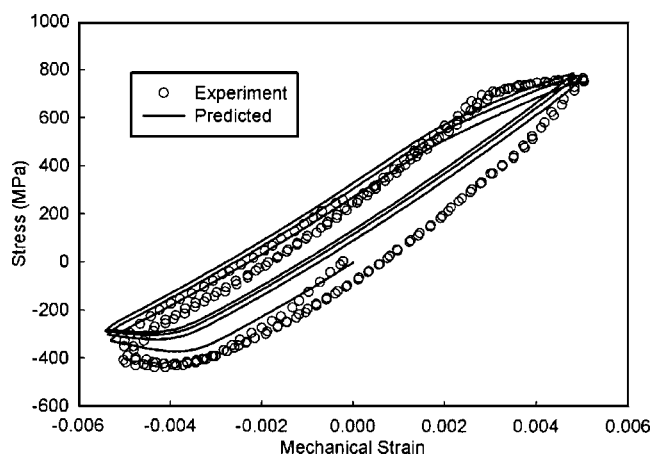


Fig. 11 Stress-strain response: comparison of experimental data with model predictions for out-of-phase (OP) TMF 538°C–927°C in the longitudinal orientation

non-isothermal fatigue conditions for purposes of predicting fatigue crack initiation life. Several isothermal fatigue (IF) and TMF life prediction models have been developed to predict the service

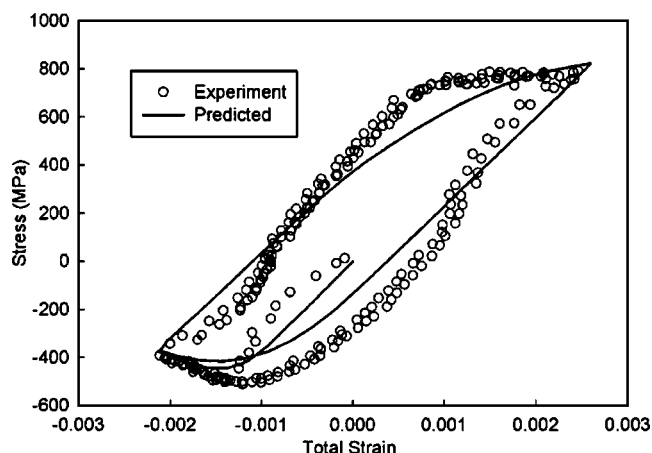


Fig. 12 Stress-strain response: comparison of experimental data with model predictions for out-of-phase (OP) TMF 538°C–927°C in the transverse orientation

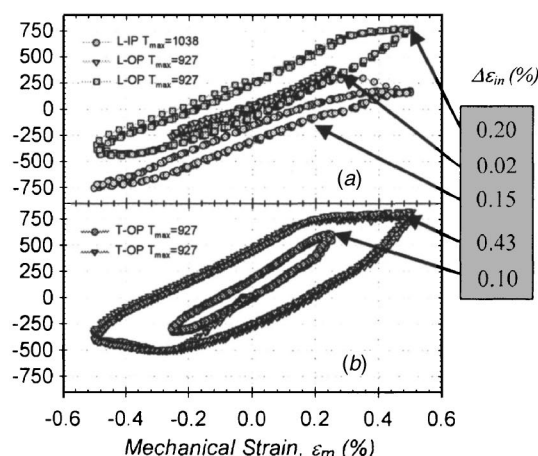
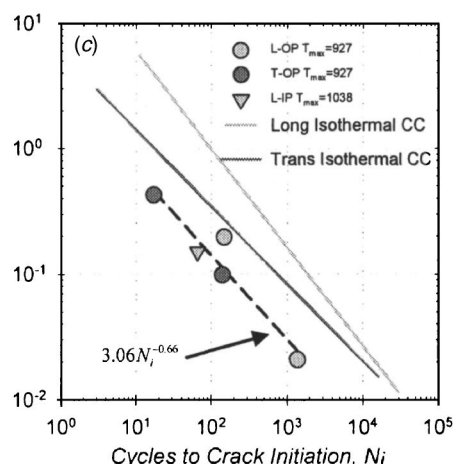


Fig. 13 Initial stress-mechanical strain responses of TMF cycled (a) longitudinal and (b) transverse specimens. (c) Inelastic strain versus fatigue crack initiation lives for TMF and LCF experiments at 871°C

lives of turbine blade materials subjected to high homologous temperatures [32–39]. The approaches that have been developed are categorized as energy-based, strain-based, and damage based. Coffin [32] modified the Coffin-Manson law to include environmental effects via a cycle frequency factor. Neu and Sehitoglu [33] extended Coffin-Manson concepts in a strain-based strategy to address coupled cyclic plastic strain, creep, and oxidation damage mechanisms. An energy-based approach was presented by Ostergren [34] and later modified by Zamrik and Renaud [35] and included the monotonic tensile elongation and ultimate strength data as functions of temperature. The model introduced by Rémy et al. [37] is restricted to a microstructurally small volume element adjacent to an oxidized crack tip of a CT-type specimen; in this case, the critical fracture stress of the alloy and the oxidized alloy are required. Miller et al. [38] extended damage rate equations discussed by McDowell et al. [39] for small fatigue crack propagation under thermo mechanical loading to address coupled fatigue, creep, and oxidation effects in Ni-base superalloys. Most of these models were developed for isotropic polycrystalline (PC) materials in which creep damage mechanisms such as void growth and grain boundary slip were dominant. In this paper, a crack initiation model is presented based on the observed damage mechanisms for DS GTD-111.

7.1 Observations. The stress response of DS GTD-111 under TMF is plotted with respect to the mechanical strain ϵ_m (total strain less thermal strain) for several test cases in Figs. 13(a) and 13(b). Figure 13(c) plots the inelastic strain range (mechanical strain less elastic strain) versus the number of cycles to crack initiation, $\Delta\epsilon_{in}$ versus N_i , for in-phase (IP) and out-of-phase (OP) TMF cases. The mechanisms for crack initiation change with loading history; however, no significant change in the initiation mechanism is observed with change in orientation (longitudinal versus transverse).

Three primary damage mechanisms are identified: fatigue, creep-fatigue, and oxidation-fatigue damage. A single stage II major crack is observed in the isothermal fatigue tests without hold times at all temperatures, with very little secondary cracking. At lower temperatures ($\leq 650^\circ\text{C}$), cracks initiate at cracked carbide inclusions near the surface as shown in Fig. 14(a). Initiation at higher temperatures occurs at the specimen surface from an oxide spike along the interdendritic region, as shown in Fig. 14(b). Carbide inclusions near the surface act as diffusion short circuits, thus serving as preferential sites for oxidation. A softer γ , depleted layer exists below the oxide layer further from the surface due to diffusion of aluminum. For the isothermal fatigue tests with hold



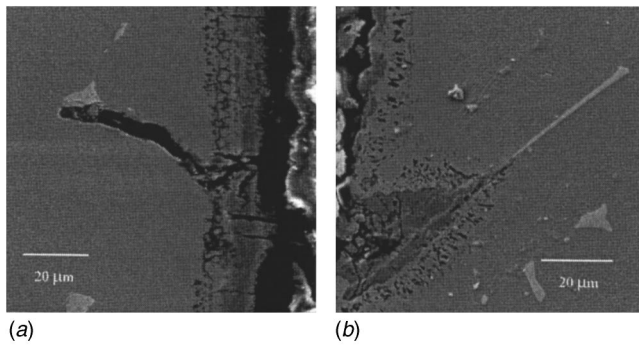


Fig. 14 (a) Crack initiation at a subsurface carbide and (b) crack initiation at the surface due to an oxide spike

times (2 min tension or compression), multiple voids are observed around γ/γ' eutectic nodules where crack initiation takes place, thus, indicating a creep degradation mechanism. From Table 3, the crack initiation life is shorter in longitudinal oriented specimen in the tests with hold time as compared to those without hold times due to the contribution from a creep component in addition to the fatigue and oxidation components. This is not true in the transverse orientation at higher temperatures ($>871^\circ\text{C}$) where the hold times in compression give higher crack initiation lives. More experimental tests will be conducted and fatigue specimens will be analyzed as a part of future work to understand this anomalous behavior in the transverse orientation at higher temperatures. In the TMF tests, the material microstructure plays a much more important role in the IP tests as compared to the OP tests. MC carbide inclusion cracking is observed near the specimen surface in the IP tests and some voids are also observed around the γ/γ' eutectic nodules. Oxide spiking is the primary mode of crack initiation in the OP TMF tests and oxide spallation is also observed but to a much smaller extent.

7.2 Creep-Fatigue-Environment Crack Initiation Model.

The model in this section is based on application of the TMF model developed by Neu and Sehitoglu [33]. Assuming a unique relationship between the damage fraction and cycle fraction with respect to cycles to crack initiation for each damage mode, the total crack initiation life can be represented in terms of the individual damage components (fatigue, creep-fatigue, and oxidation-fatigue, respectively), and can be written as [33]

$$\frac{1}{N_{\text{tot}}} = \frac{1}{N_{\text{fat}}} + \frac{1}{N_{\text{cr}}} + \frac{1}{N_{\text{ox}}} \quad (16)$$

Relationships for each of these components are determined by conducting LCF and TMF tests to isolate the damage mechanisms. Mathematical formulations are developed to relate each mechanism to temperature, grain orientation, hold times, etc. The fatigue damage mechanism is governed by [33]

$$N_i^{\text{fat}} = C_1 f_1 (\Delta \varepsilon_{\text{in}})^{C_2} \quad (17)$$

where C_1 and C_2 are constants, and f_1 is a factor that accounts for material orientation with respect to the applied loading direction (i.e., L or T). To characterize this relation, data are needed from low temperatures, high strain rates, and CC tests. Tests conducted at and below 871°C are used to correlate Eq. (17). The creep-fatigue interaction mechanism is found to correlate to

$$N_i^{\text{cr}} = C_3 \Theta_{\text{cr}}(T, t) \left(\frac{t_c + t_h}{t_c + 2t_h} \right)^{f_2} (\Delta \varepsilon_{\text{in}})^{C_4} \quad (18)$$

where C_3 , C_4 , and f_2 are constants [33]. The inelastic strain range, $\Delta \varepsilon_{\text{in}}$, is used here since it captures orientation and time-dependent deformation. The diffusion coefficient, Θ_{cr} , along with the cycle and dwell times, given by t_c and t_h , respectively, account for time and temperature-dependent degradation mechanisms such as internal void nucleation and growth that are not captured by Eq. (17). The diffusion term is given by

$$\Theta_{\text{cr}}(T, t) = \frac{1}{t_c} \int_0^{t_c} \exp\left(-\frac{Q_{\text{cr}}}{RT(t)}\right) dt \quad (19)$$

Here Q_{cr} is the activation energy, $T(t)$ is the temperature history, and R is the universal gas constant. Specimens subjected to dwell times experience the most significant stress relaxation induced by viscoplastic deformation. The correlation of Eq. (18) involves HT and HC tests at or above 871°C .

The term relating oxidation-fatigue interaction to crack initiation is motivated by the oxide spiking mechanism. The interaction is related to cycle-dependent repeated fracture of the oxide film. This process is controlled by the elastic part of the mechanical strain range, $\Delta \varepsilon_{\text{el}}$, the oxidation growth kinetics, and the phasing between the mechanical and thermal loading captured through a phasing factor, Φ_{ox} , i.e.,

$$N_i^{\text{ox}} = C_5 [\Phi_{\text{ox}} \Theta_{\text{ox}}(t_c + t_h)]^{C_6} \Delta \varepsilon_{\text{el}}^{C_7} \quad (20)$$

Here C_5 , C_6 , and C_7 are constants [33]. The diffusion factor, Θ_{ox} , in analogy to Eq. (19) for creep, captures the oxide film growth kinetics. The phasing factor is given by

$$\Phi_{\text{ox}} = \exp[-C_8(\dot{\varepsilon}_{\text{th}}/\dot{\varepsilon}_m + 1)^2] \quad (21)$$

This factor has a maximum value of unity for linear OP TMF, the condition most susceptible to the oxide spiking mechanism. Hysteresis data from isothermal tests above 871°C , along with dwells and TMF tests, are used to determine the constants for Eqs. (20) and (21). Constants are summarized in Table 5.

7.3 Model Correlation and Predictions. Some trends predicted by the model are shown in Fig. 15 for continuously cycled longitudinally oriented DS GTD-111 specimens. For both isothermal (Fig. 15(a)) and nonisothermal (Fig. 15(b)) cases, the crack initiation life is characterized by the stress-strain response at high mechanical strain ranges since the fatigue term dominates.

Under isothermal conditions, the change in slope of predicted life below the mechanical strain range of 1.0% relates to a transition from predominantly fatigue to a coupling of oxidation and

Table 5 Constants for the crack initiation model

Fatigue Term		Creep-Fatigue Term		Environment-Fatigue Term	
Symbol	Value	Symbol	Value	Symbol	Value
C_1	0.15	C_3	60	C_5	0.10
C_2	-0.65	C_4	-1.10	C_6	-0.57
f_1	0.78	f_2	1.00	C_7	-0.45
		Q_{cr} (KJ/mol)	6.75	C_8	0.50
				Q_{ox} (KJ/mol)	164

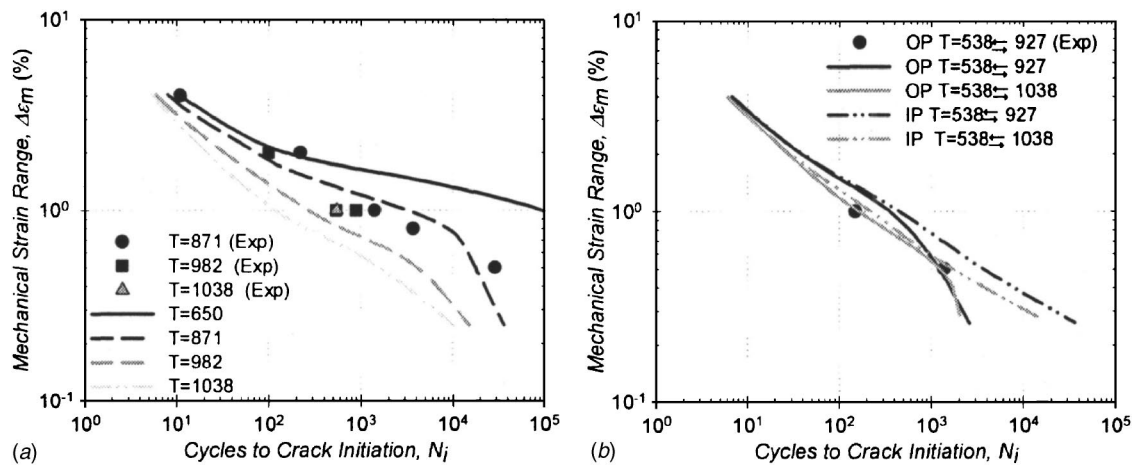


Fig. 15 Predicted trends and selected experimental results for (a) isothermal LCF and (b) TMF of longitudinal DS GTD111 under CC

fatigue mechanisms. As the temperature is decreased below 871°C, there is insufficient thermodynamic driving force for oxidation and the role of environment is limited as a result. Under TMF conditions at lower mechanical strain ranges (Fig. 15(b)), the OP cycle is predicted to be more damaging than the IP cycle. This prediction is consistent with experiments since the oxide spiking, which is more detrimental to life than oxide spallation, is experienced during OP cycling. During IP cycling with $\Delta\epsilon_m < 1.0\%$, life is dominated by the fatigue mechanism. With the increase of ΔT from 389°C to 500°C, the constitutive model predicts $\Delta\epsilon_{in}$ to increase. Tests conducted at same temperature and total strain amplitudes on longitudinal and transverse oriented DS GTD-111 specimens lead to larger inelastic strain ranges for transverse specimens since transverse specimens have a larger elastic stiffness (Figs. 6 and 7). Consequently, the lives of longitudinal specimens typically outlast those of transverse specimens when tested at the same total strain range. The crystallographic orientation dependence in the constitutive model captures this phenomenon, predicting the trends especially at the higher mechanical strain ranges.

8 Summary

The deformation and failure mechanisms occurring in a directionally solidified Ni-base superalloy, DS GTD-111, have been characterized as a function of temperature and loading history. A continuum crystal plasticity model is developed to characterize the material behavior in the longitudinal and transverse orientations. Isothermal and thermomechanical uniaxial fatigue tests with hold times and creep tests are conducted at temperatures ranging from room temperature (RT) to 1038°C to characterize the deformation response. Using isothermal test data to fit constants, IP and OP TMF responses are adequately predicted. The fatigue specimens are studied to identify the damage mechanisms and a physically based model for predicting crack initiation life is developed based on the experimental stress-strain data. Three primary damage mechanisms are identified: fatigue, creep-fatigue, and oxidation-fatigue induced damage. Crack initiation life predictions, based on the life models for each damage mechanism, follow the experimental trends.

Acknowledgment

The author acknowledges the help from Matt Trexler, Garry Donaghy, and Tam Nguyen.

References

- [1] Meric, L., Poubanne, P., and Cailletaud, G., 1991, "Single Crystal Modeling

- for Structural Calculations Part I—Model Presentation," *J. Eng. Mater. Technol.*, **162**(113), pp. 162–170.
- [2] Trexler M., and Sanders, T., 2002, personal communication, Georgia Institute of Technology.
- [3] Westbrook, J. H., 1996, "Superalloys (Ni base) and dislocations—An Introduction," *Dislocat. Solids*, **10**, pp. 1–25.
- [4] Lall, C., Chin, S., and Pope, D., 1979, "Orientation and temperature dependence of the yield stress of Ni3 (al, nb) single crystals," *Metall. Trans. A*, **10A**, pp. 1323.
- [5] Paidar, V., Pope, D. P., and Vitek, V., 1984, "A theory of the anomalous yield behavior in Li_2 ordered alloys," *Acta Metall.*, **32**(3), pp. 435–448.
- [6] Umakoshi, Y., Pope, D. P., and Vitek, V., 1984, "The asymmetry of the flow stress in Ni3 (Al, Ta) single crystals," *Acta Metall.*, **32**(3), pp. 449–456.
- [7] Osterle, W., Bettge, D., Fedelich, B., and Klingelhoefer, K., 2000, "Modelling the orientation and direction dependence of the critical resolved shear stress of Nickel-base superalloy single crystals," *Acta Mater.*, **48**, pp. 689–700.
- [8] Jiao, F., Bettge, D., Osterle, W., and Ziebs, J., 1996, "Tension compression asymmetry of the (001) single crystal superalloy SC16 under cyclic loading at elevated temperatures," *Acta Metall.*, **44**(10), pp. 3933–3942.
- [9] Vitek, V., Pope, D. P., and Bassani, J. L., 1996, "Superalloys (Ni base) and dislocations—An Introduction," *Dislocat. Solids*, **10**, pp. 135–186.
- [10] Lee, E. H., 1969, "Elastic-Plastic Deformations at Finite Strains," *ASME J. Appl. Mech.*, **36**, pp. 1–6.
- [11] Sheh, M. Y., and Stouffer, D. C., 1988, "Anisotropic Constitutive model for Nickel-base Single Crystal Superalloys," NASA Report No. CR-182157.
- [12] Bilby, B., Bullough, R., and Smith, E., 1955, "Continuous Distributions of Dislocations: A New Application of the Methods of Non-Riemannian Geometry," *Proc. R. Soc. London, Ser. A*, **231**, pp. 263–273.
- [13] Takeuchi, S., and Karamoto, E., 1971, "Anomalous temperature dependence of the yield stress in Ni3Ga," *J. Phys. Soc. Jpn.*, **31**, pp. 1282.
- [14] Takeuchi, S., and Karamoto, E., 1973, "Temperature and Orientation Dependence of the Yield Stress in Ni3Ga Single Crystals," *Acta Metall.*, **21**, pp. 415–425.
- [15] Hirsch, P. B., 1992, "A new theory of the anomalous yield stress in Li_2 alloys," *Philos. Mag. A*, **62**(3), pp. 569–612.
- [16] Sun, Y. Q., and Hazzledine, P. M., 1996, "Geometry of dislocation glide in Li_2 γ' -phase: TEM observations," *Dislocat. Solids*, **10**, pp. 27–68.
- [17] Qin, Q., and Bassani, J. L., 1992, "Non-Schmid yield behavior in single crystals," *J. Mech. Phys. Solids*, **40**(4), pp. 813–833.
- [18] McDowell, D. L., 1992, "A nonlinear kinematic hardening theory for cyclic thermoplasticity and thermoviscoplasticity," *Int. J. Plast.*, **8**, pp. 695–728.
- [19] Castelli, M. G., and Ellis, J. R., 1993, "Improved techniques for thermomechanical testing in support of deformation modeling," *Symposium on Thermomechanical Fatigue Behavior of Materials (STP 1186)*, Sehitoglu, J. (Ed.), San Diego, CA, ASTM, pp. 195–211.
- [20] ASTM E-606-92, 2001, "Standard Practice for Strain-Controlled Fatigue Testing," ASTM, West Conshohocken, PA.
- [21] ASTM E2368, 2004, "Standard Practice for Strain-Controlled Thermomechanical Fatigue Testing," ASTM International.
- [22] ABAQUS, 2003, Hibbitt, Karlsson, and Sorensen, Inc., Providence, RI, v6.3.
- [23] McGinty, R. D., 2001, "Multiscale Representation of Polycrystalline Inelasticity," Ph.D. thesis, Georgia Institute of Technology.
- [24] Bettge, D., and Osterle, W., 1999, "Cube Slip in Near-[111] Oriented Specimens of a Single-Crystal Nickel-Base Superalloy," *Scr. Mater.*, **40**(4), pp. 389–395.
- [25] Mielek, J., Novak, V., Zarubova, N., and Gemberle, A., 1997, "Orientation Dependence of Plastic Deformation in NiAl Single Crystals," *Mater. Sci. Eng., A*, **234–236**, pp. 410–413.
- [26] Daleo, J. A., and Wilson, J. R., 1998, "GTD-111 Alloy Material Study," *J.*

- engineering for gas turbines and power, 120, pp. 375–382.
- [27] Tanner, A. B., McGinty, R. D., and McDowell, D. L., 1999, “Modeling Temperature and Strain Rate Sequence Effects on OFHC Copper,” *Int. J. Plast.*, **15**, pp. 575–603.
 - [28] Epogy, Synaps Inc., 2004, Atlanta, GA, USA, v2004A.
 - [29] Ferney, V., Hautefeuille, M., and Clavel, M., 1991, “Multiaxial Cyclic Behavior in Two Precipitates Strengthened Alloys: Influence of the Loading Path and Microstructure,” *Mem. Etud. Sci. Rev. Metall.*, **88**, pp. 441–451.
 - [30] Latif, A., Clavel, M., Ferney, V., and Saanouni, A., 1994, “On the Modeling of Non-Proportional Cyclic Plasticity of Waspaloy,” *ASME J. Eng. Mater. Technol.*, **116**, pp. 35–44.
 - [31] Shrikanth, A., and Zabaraz, N., 1999, “A Computational Model for the Finite Element Analysis of Thermoplasticity Coupled with Ductile Damage at Finite Strains,” *Int. J. Numer. Methods Eng.*, **45**, pp. 1569–1605.
 - [32] Coffin, L. F., 1977, *Fatigue at High Temperature*, Fourth International Conference on Fracture, Pergamon Press, Waterloo, Ont., Canada.
 - [33] Neu, R. W., and Sehitoglu, H., 1989, “Thermomechanical Fatigue, Oxidation and Creep: Part II Life Prediction,” *Metall. Trans. A*, **20A**, pp. 1769–1783.
 - [34] Ostergren, W. J., 1992, “A Damage Function and Associated Failure Equations for Predicting Hold Time and Frequency Effects in Elevated Temperature, Low-Cycle Fatigue,” *J. Test. Eval.*, **4**(5), pp. 327–339.
 - [35] Zamrik, S. Y., and Renaud, M. L., 2000, “Thermo-Mechanical Out-of-Phase Fatigue Life of Overlay Coated IN-738LC Gas Turbine Material,” *Thermomechanical Fatigue Behavior of Materials: Third Volume*, ASTM 1371, H. Sehitoglu, and H. J. Maier, Eds., American Society for Testing and Materials, Philadelphia, pp. 119–137.
 - [36] Bernstein, H. L., Grant, T. S., McClung, R. C., and Allen, J. M., 1993, “Prediction of Thermal Mechanical Fatigue Life for Gas Turbine Blades in Electric Power Generation,” *Thermomechanical Fatigue Behavior of Materials*, ASTM STP 1186, H. Sehitoglu, Ed., ASTM, West Conshohocken, PA, pp. 212–238.
 - [37] Rémy, L., Bernard, H., Malpertu, J. L., and Rezai-Aria, F., 1993, “Fatigue Life Prediction Under Thermal-Mechanical Loading in a Nickel-Base Superalloy,” in *Thermomechanical Fatigue Behavior of Materials*, ASTM STP 1186, H. Sehitoglu, Ed., ASTM, West Conshohocken, PA, pp. 3–16.
 - [38] Miller, M. P., McDowell, D. L., and Oehmke, R. L. T., 1992, “A Creep-Fatigue-Oxidation Microcrack Propagation Model for Thermomechanical Fatigue,” *ASME J. Eng. Mater. Technol.*, **114**(3), pp. 282–288.
 - [39] McDowell, D. L., Antolovich, S. D., and Oehmke, R. L. T., 1992, “Mechanistic Considerations for TMF Life Prediction of Nickel-Base Superalloys,” *Nucl. Eng. Des.*, **133**, pp. 383–399.